Journal of Physics: Condensed Matter

ACCEPTED MANUSCRIPT

Origin of the magnetic transition at 100 K in ε-Fe_2O_3 nanoparticles studied by X-ray absorption fine structure spectroscopy

To cite this article before publication: Jesus Lopez Sanchez *et al* 2017 *J. Phys.: Condens. Matter* in press https://doi.org/10.1088/1361-648X/aa904b

Manuscript version: Accepted Manuscript

Accepted Manuscript is “the version of the article accepted for publication including all changes made as a result of the peer review process, and which may also include the addition to the article by IOP Publishing of a header, an article ID, a cover sheet and/or an ‘Accepted Manuscript’ watermark, but excluding any other editing, typesetting or other changes made by IOP Publishing and/or its licensors”

This Accepted Manuscript is **© 2017 IOP Publishing Ltd**.

During the embargo period (the 12 month period from the publication of the Version of Record of this article), the Accepted Manuscript is fully protected by copyright and cannot be reused or reposted elsewhere.
As the Version of Record of this article is going to be / has been published on a subscription basis, this Accepted Manuscript is available for reuse under a CC BY-NC-ND 3.0 licence after the 12 month embargo period.

After the embargo period, everyone is permitted to use copy and redistribute this article for non-commercial purposes only, provided that they adhere to all the terms of the licence https://creativecommons.org/licences/by-nc-nd/3.0

Although reasonable endeavours have been taken to obtain all necessary permissions from third parties to include their copyrighted content within this article, their full citation and copyright line may not be present in this Accepted Manuscript version. Before using any content from this article, please refer to the Version of Record on IOPscience once published for full citation and copyright details, as permissions will likely be required. All third party content is fully copyright protected, unless specifically stated otherwise in the figure caption in the Version of Record.

View the article online for updates and enhancements.

This content was downloaded from IP address 159.149.98.176 on 05/10/2017 at 14:19

Origin of the magnetic transition at 100 K in ε-Fe_2O_3 nanoparticles studied by X-ray absorption fine structure spectroscopy

J. López-Sánchez,[1,2*] A. Muñoz-Noval,[3,4], C. Castellano, [5] A. Serrano, [3,6] A. del Campo,[6] M. Cabero,[1,7] M. Varela,[1,7] M. Abuín,[1,8] J. de la Figuera,[2,9] J.F. Marco,[2,9] G. R. Castro,[3] O. Rodríguez de la Fuente,[1,2,10] N. Carmona[1,2,10]

1 Departamento de Física de Materiales, Universidad Complutense de Madrid, 28040 Madrid, Spain.
2 Unidad Asociada IQFR (CSIC)-UCM, 28040 Madrid, Spain.
3 Spanish CRG, The European Synchrotron (ESRF), 38000 Grenoble, France and Instituto de Ciencia de Materiales de Madrid, ICMM-CSIC, 28049 Madrid, Spain.
4 Department of Applied Chemistry, Hiroshima University, Higashihiroshima, Hiroshima, 739-8527, Japan.
5 Dipartimento di Chimica, Universitá degli Studi di Milano, 20133 Milano, Italy.
6 Instituto de Cerámica y Vidrio, ICV-CSIC, 28049 Madrid, Spain.
7 Instituto Pluridisciplinar, Universidad Complutense de Madrid. 28040, Madrid. Spain
8 CEI Campus Moncloa, UCM-UPM, 28040 Madrid, Spain
9 Instituto de Química Física "Rocasolano", CSIC, 28006 Madrid, Spain.
10 Instituto de Magnetismo Aplicado, UCM-CSIC-ADIF, 28230 Las Rozas, Madrid, Spain.

*Corresponding author: jesus.lopez@ucm.es

Abstract

The current study unveils the structural origin of the magnetic transition of the ε-Fe_2O_3 polymorph from an incommensurate magnetic order to a collinear ferrimagnetic state at low temperature. The high crystallinity of the samples and the absence of other iron oxide polymorphs have allowed us to carry out temperature-dependent X-ray absorption fine structure spectroscopy experiments out. The deformation of the structure is followed by the Debye-Waller factor for each selected Fe-O and Fe-Fe sub-shells. For nanoparticle sizes between 7 and 15 nm, the structural distortions between the Fe_{te} and Fe-$D1_{oc}$ sites are localized in a temperature range before the magnetic transition starts. On the contrary, the inherent interaction between the other sub-shells (named Fe-O1,2 and Fe-Fe1) provokes cooperative magneto-structural changes in the same temperature range. This means that the Fe_{te} with Fe-$D1_{oc}$ polyhedron interaction seems to be uncoupled with temperature dealing with these nanoparticle sizes wherein the structural distortions are likely moderate due to surface effects.

1. Introduction

ε-Fe_2O_3 is a collinear ferrimagnetic material which presents a Curie transition at ~500 K and an incommensurate magnetic order transition at ~100 K at the nanoscale [1]. Concerning its magnetic properties, single-domain ε-nanoparticles exhibit a coercive field of 20 kOe at room temperature (RT). The origin of this high value is its huge magnetocrystalline anisotropy ($K=10^5$ J/m^3) originated by a nonzero orbital component of the Fe^{3+} magnetic moment and consequently, the occurrence of a strong spin-orbit coupling [2]. In this respect, a new generation of hard-magnets without rare-earth compounds based on this kind of Fe oxides seems to be feasible [3]. Furthermore, this material has the potential to be employed in high speed wireless communication technologies, since the ferromagnetic resonance frequency falls within the mTHz range [2],[4],[5]. In addition to the above-mentioned features, ε-Fe_2O_3 is a semiconductor material with a gap of 1.9 eV [6] and presents coupling between magnetic and dielectric properties [7]. Specifically, interesting properties are also found in thin film form, for layers with a few tens of nanometers. In these systems, apart from ferrimagnetic behavior, epsilon also displays a ferroelectric response at room temperature (RT) [8].

Motivated by these outstanding properties, several synthesis methods have been developed to achieve high crystalline quality thin films, i.e. Pulsed Laser Deposition (PLD) [8,9], Chemical Vapor Deposition (CVD) [10], sol-gel [11–20] and reverse micelle and sol-gel combined method [21–25]. Sol-gel stands out among all other processes due to the possibility of tuning the morphology and size of the micro- and nanostructures, the high chemical homogeneity, size monodispersity according to experimental conditions and industrial scalability [26]. The present work is based on a novel one-pot sol-gel synthesis route for obtaining ε-Fe_2O_3 particles embedded in SiO_2 films explained in detail in a previous work [16] and which has been modified for this experiment. The new recipe is assisted by one polyalcohol (glycerol), which provides a steric shielding around the colloidal particles (sols) during the hydrolysis and polycondensation stages [27,28] and maintains them stabilized during the final thermal treatment at high temperatures.

The reported samples contain the ε-phase with a nominal concentration of 100% of the total Fe oxide content. To our best knowledge, this is the highest ε-content ever achieved in the form of a thin film prepared by the sol-gel method. This fact permits to investigate, for the first time with X-ray absorption fine structure technique (XAFS), the low temperature magnetic anomaly at 100 K previously observed for this iron oxide phase with other experimental techniques [14,29–31]. According to previous neutron powder diffraction (NPD) and X-ray diffraction (XRD) experiments [30], there are structural distortions, mainly in the local coordination of one of the Fe octahedral distorted sites (Fe-$D1_{oc}$) and in the Fe tetrahedral sites (Fe_{te}), associated to a transition from a collinear ferrimagnet order to an incommensurate magnetic order. However, the limitations of XRD to inspect the closest environment of the atom hinders the confirmation of this last point. In this regard, the very local nature of XAFS can offer new clues about the nature of this magnetic anomaly. XAFS of a selected element is highly sensitive to its coordination number, neighbor distances, oxidation state and nature of the neighbors. Since this magnetic transition involves structural modifications in specific Fe^{3+} sites, a plausible relation to structural distortions in the octahedral and tetrahedral sites is investigated in this work.

2. Experimental section

Growth of the films: Continuous films are reproducibly synthesized by the sol-gel method. An hydroethanolic solution is elaborated adding iron nitrate nonahydrate ($Fe(NO_3)_3.9H_2O$, Sigma-Aldrich >98 %), barium nitrate ($Ba(NO_3)_2$, Sigma-Aldrich >98 %) and TEOS (Sigma-Aldrich >98 %) in a 1 : 0.02 : 1 molar ratio. The prepared sol is mixed under vigorous stirring and some drops of glycerol (Sigma-Aldrich >99,5 %) is added to help hydrolysis and polycondensation. The films are deposited by dip-coating on Si(100) substrates with a constant speed of 2.56 mm/s. The processed films are dried for several days at 340 K. Then, a subsequent thermal treatment up to 1230 K is carried out in order to obtain the final crystalline state.

Material characterization: Surface characterization is performed using a Nanotec atomic force microscope (AFM) operating in dynamic mode in air. AFM images are analyzed using the WSxM software [32]. The morphological structure of the films is investigated by scanning electron microscopy (SEM) with a CRESTEC CABL-9500C instrument. The crystalline structure was studied by XRD with a PANalytical Philips X'Pert Pro MRD diffractometer using Cu Kα radiation (λ = 1.542 Å) and high resolution scanning transmission electron microscopy (STEM) images are acquired by using an electron microscope JEOL ARM200 equipped with a spherical aberration corrector. The structural and chemical environments of the Fe^{3+} ions are studied by integral conversion electron Mössbauer spectroscopy (ICEMS) and X-ray absorption spectroscopy (XAS). ICEMS data are acquired at RT in a conventional constant acceleration spectrometer using a $^{57}Co(Rh)$ source and a parallel plate avalanche counter. All the chemical isomer shifts data are referred to the centroid of the spectrum of α-Fe at RT. Complementary measurements are also carried out using a Witec ALPHA 300RA confocal Raman microscope (CRM) with a Nd:YAG green laser (532 nm) in p-polarization.

Magnetic properties of the films are also examined with a quantum design MPMS-XL magnetometer (SQUID). Hysteresis magnetic loops at RT are obtained with a maximum applied magnetic field of 5 T and field-cooling (FC) and zero-field-cooling (ZFC) curves are collected in the temperature range 5-300 K under 50 kOe and 200 Oe respectively.

XAFS measurements are carried out at the Fe K-edge (7112 eV) in fluorescence yield mode in the range between 6900 and 8000 eV at the SpLine BM25A Spanish beamline of the ESRF synchrotron in Grenoble (France). Signals are collected using a 13 element Si(Li) solid state detector (INCA, Sgx Sensortech). BM25A beamline optics accounts with a double Si(111) X-ray monochromator for the diffraction and absorption bending magnet beamline at the ESRF [33]. Spectra are acquired at 15 different temperatures in the range of 10 to 298 K. An Oxford CV-F Optistat liquid helium cryostat with a LHe Dewar supply is used to cool down the sample. XAFS data are reduced applying standard procedures using the Demeter package [34]. Fits on k^3 weighted signals are carried out simultaneously in the module, real and imaginary parts of the Fourier transform of the extended X-ray absorption fine structure (EXAFS) spectra in R space using theoretical functions from FEFF8.4 code [35,36]. The calculations of the paths are performed by FEFF using a crystallographic standard reference [36]. For the model, we apply the maximum number of paths corresponding to single scattering in agreement with the experimental resolution, applying the criteria $\delta R \cong \pi / 2k_{max}$.

In the case that two paths have distances whose difference is beyond the resolution limit, they cannot be resolved individually. This is the criterion applied in the calculations of the structural parameters of each atomic shell. In our case, we experimentally reached *k* values of 10.5 Å^{-1} with acceptable quality, but we restrict the value even down to 8.7 Å^{-1} to keep the experimental signal-to-noise ratio at a minimum. Thus, according to this limitation, the minimum distance for distinguishable paths is 0.18 Å. In the model, two main O shells are introduced and are composed by 4 and 1 O atoms and two Fe shells with 8 and 2 atoms, respectively. The fittings are performed in the 1-3.5 Å real space range. The EXAFS amplitude factor is obtained from the fitting of the lowest temperature condition and kept fixed for the whole series. The non-structural parameter (energy shift *E*) is also constrained within a short range of values, based on the calculations of the first condition to allow their variation during the convergence. So, the fitted parameters are the relative displacement of the bonding distance (a global parameter that accounts for variation of the experimental atomic shell distance from the tabulated in the path calculation) and the Debye-Waller (DW) factors of the four main atomic shells considered.

3. Results and discussion

Morphological characterization

The roughness and morphology of the films are determined by SEM and AFM (Figure 1). The root mean square (RMS) roughness of the films is 0.58 nm. This means that the nanoparticles, with small sizes, are homogenously distributed in the sample. This is a consequence of enhancing thin film porosity and increasing solution viscosity by the glycerol addition [27].

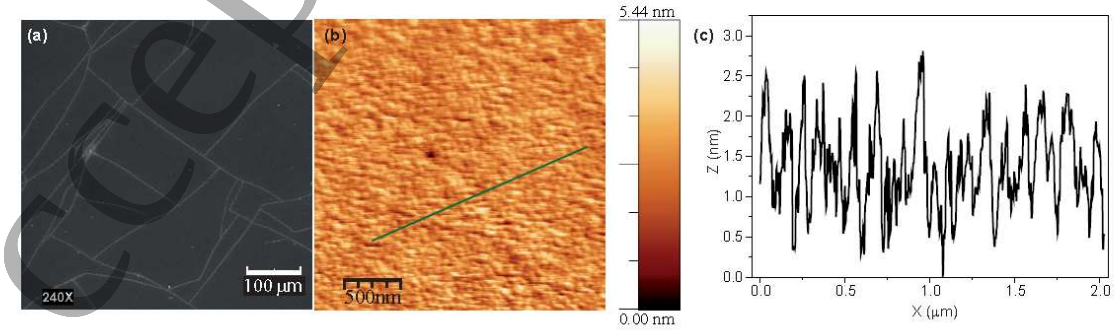

Figure 1: (a) SEM and (b) AFM images of the thin films with ε-Fe_2O_3 nanoparticles embedded in a SiO_2 matrix prepared at 1230 K; (c) AFM Z-profile corresponding to the green line marked in Figure (b).

The final thickness of the films, measured by AFM, is around 200 nm. Fractures or cracks in thin film samples prepared by sol-gel are a common issue, and to avoid them glycerol is widely employed as an additive [28]. But even with this precursor, fractures along the surface of the film are produced during the final thermal treatment (see Figure 1a). Several AFM images are acquired by dynamic mode and they show the same morphology and nanostructure of the film. Therefore, homogeneous smooth surfaces with low surface roughness values are achieved.

The XRD measurements are carried out in grazing incidence to enhance surface sensitivity (see Figure 2). Different grazing incidence angles (ω) are tested in order to get the best experimental conditions. Figure 2 shows a diffraction pattern of the sample grown on a Si(100) substrate right after the deposition of the coating (lower black line), and after the high temperature synthesis step at 1230 K (upper blue line). The latter displays a polycrystalline epsilon iron oxide signal [37], the substrate contribution and one pronounced bump contribution. The origin of this bump detected at low angles is attributed to amorphous SiO_2 signal of the matrix [12], where the ε-nanoparticles are embedded.

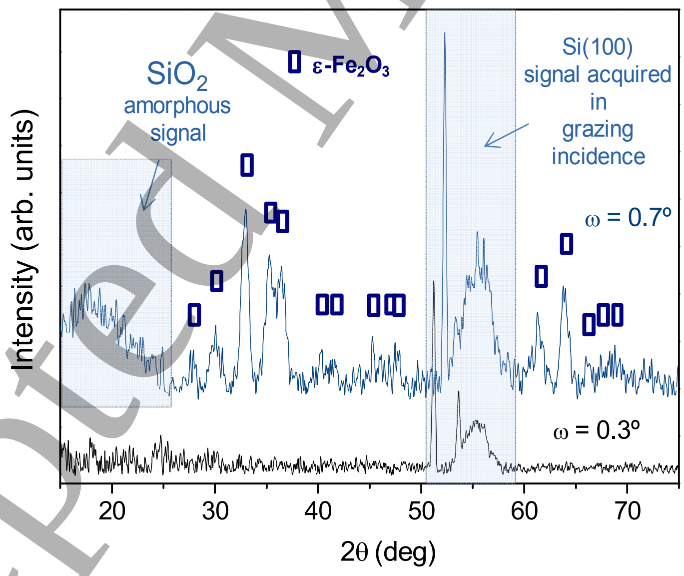

Figure 2. XRD patterns of a typical Si(100) substrate (lower pattern), and a sol-gel thin film sample synthesized at 1230 K (upper pattern). Diffraction peaks corresponding to the ε-polymorph are identified [37].

The ε-polymorph is a metastable phase and, so far, it is difficult to synthesize as a single phase [31,38]. Frequently, this phase is accompanied by other more stable iron oxide polymorphs, such as maghemite [11] and/or hematite [16], being this the most common coexisting phase. However, due to the resolution and signal/noise ratio of the experimental

XRD data, contributions of other iron oxides cannot be ruled out. The obtained diffraction peaks of ε-phase are broad, probably due to the nanometric size of the particles. The grain size calculated following the Debye-Scherrer equation considering a shape factor of 0.94 and assuming a spherical shape, is ∼12 nm. Therefore, we may consider that there are single magnetic domain nanoparticles with no preferred orientations arranged through the SiO_2 matrix [39].

To know the distribution of these nanoparticles into the film, high angle annular dark field (HAADF) images are recorded in different cross-section areas of the sample (see Figure 3). The iron oxide nanoparticles are distributed homogeneously along the coating (see Figures 3a-b), and these have different diameters ranging between 7 and 15 nm, approximately. Therefore, these results are in concordance with the previous Scherrer estimation and we suggest that the particle size distribution obtained is relatively sharp. Furthermore, the coating seems to be compact and presents a high concentration of nanoparticles. The porous silica matrix and the presence of glycerol might avoid the nanoparticle aggregation and maintain the particle size in the mentioned range. All these factors are crucial to conform ε-nanoparticles immerse in the silica matrix in these synthesis and thermal conditions. Figure 3c shows an oriented iron oxide nanoparticle which is located close to the bottom interface whereas other nanoparticles (not oriented) are superimposed. Structural analyses were performed to prove the nature of this specific nanoparticle and they match with the [101] oriented epsilon structure. Figure 3d displays some Fe^{3+} and O^{2-} ions arranged along the (010) projection. These data reveal that the formation of the ε-phase does not require a direct exposure to the oxygen taken from the air environment during the thermal treatment at high temperatures.

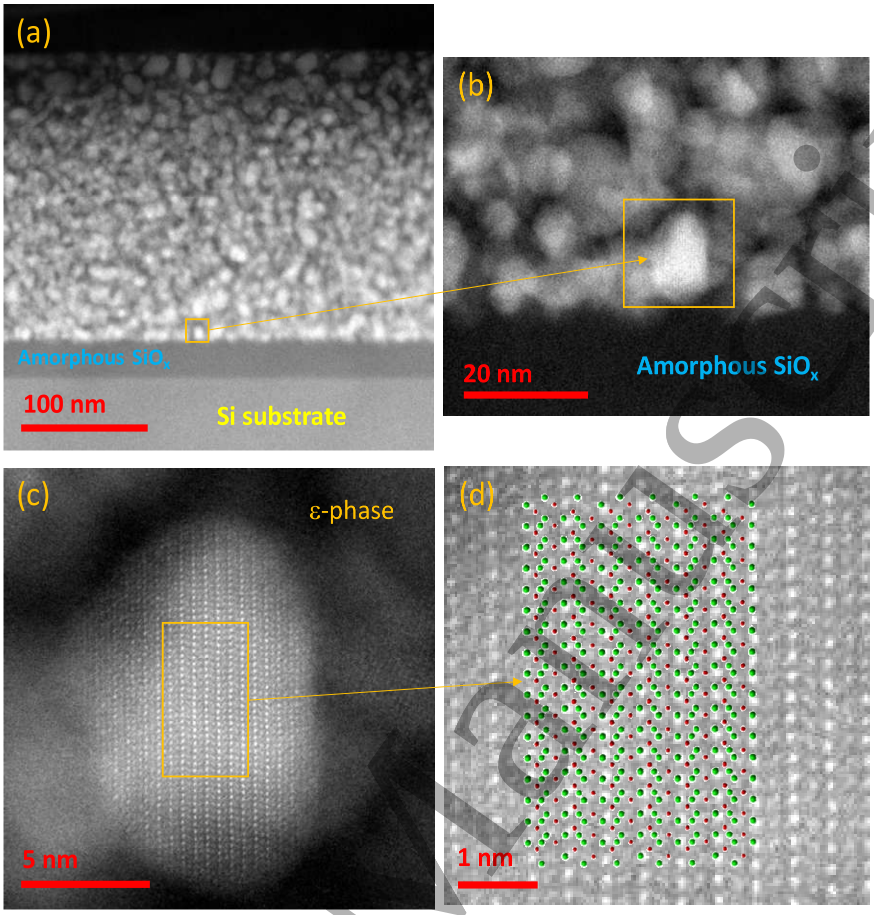

Figure 3. (a) Low magnification HAADF image of the ε-nanoparticle embedded in the silica matrix; HAADF images: (b) selected area of Figure a, (c) ε-Fe_2O_3 nanoparticle oriented down the [101] crystal plane, and (d) magnification of the yellow rectangular area where are superimposed along (010) direction some Fe^{3+} (green) and O^{2-} (red) ions (for simplicity).

The chemical environment and structural properties are also examined by Mössbauer spectroscopy. ε-Fe_2O_3 has a complex structure with four different Fe sites. Three Fe^{3+} sites have octahedral coordination: one regular (Fe-R_{oc}) and two distorted (Fe-D1,2_{oc}). The other site has a tetrahedral coordination ($Fe4_{te}$) [15] (Figure 4a). The RT Mössbauer spectrum shares three magnetic sextets and a paramagnetic doublet (see Figure 4b). The occurrence in the spectrum of three sextets instead of the expected four is due to the fact that the sextets corresponding to two of the Fe^{3+} in the octahedral sites (Fe-D1,2_{oc}) have very similar hyperfine parameters and cannot be resolved. Therefore, only one sextet is observed with a spectral area twice the expected one [40,41].

The Mössbauer spectrum displays in Figure 4b presents broad peaks over a global bump (background), which is in concordance with nanoparticle sizes. Considering the contributions of the relative areas from the Lorentzian fit, the Mössbauer parameters and the phase composition of the sample are obtained (see Table 1). Hence, Mössbauer data reveal a 100 % percentage of the ε-phase. It is true that the paramagnetic doublet might be associated with other Fe_2O_3-polymorphs. However, in such case, we should expect the magnetic characteristic sextets related to hematite [42] or maghemite [43]. Consequently, we can attribute all Mössbauer contributions to the ε-phase and, under the sensitivity of the technique, confirm the growth of a monophasic sample under these conditions.

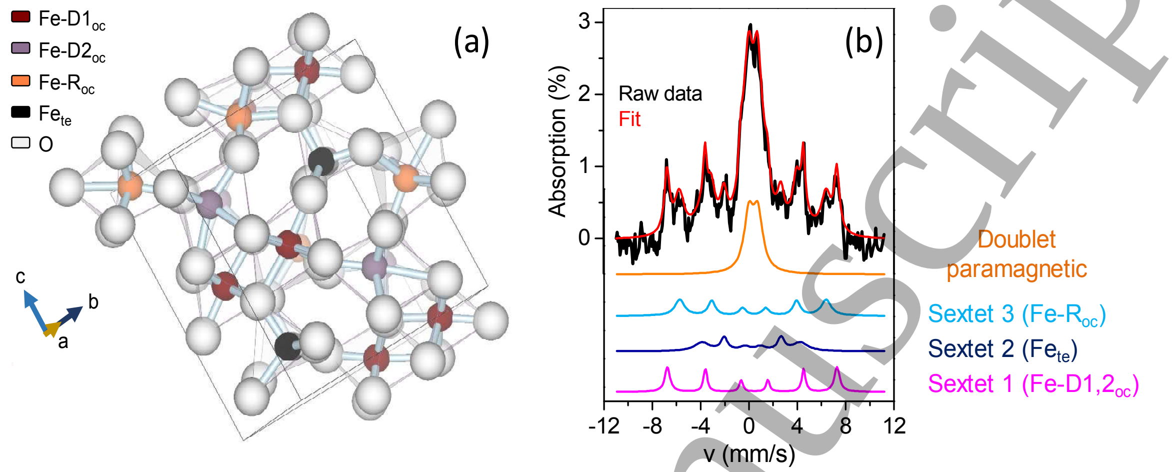

Figure 4. (a) Schematic representation of the epsilon crystal structure; (b) Mössbauer spectrum recorded at RT. Different magnetic contributions corresponding to the ε-phase are displayed at the bottom of the graph.

Table 1. Mössbauer parameters obtained from the fit of the spectrum at RT. δ is the isomer shift; Δ is the quadrupole splitting and stands for doublets; 2ε is the quadrupole shift and stands for sextets; H is the hyperfine magnetic field.

	δ (mms^{-1})	**2ε (mms^{-1})**	**H (T)**	**Area (%)**	**Assignment**
Doublet	0.36	0.75	--	39.5	ε-Fe_2O_3 SPM
Sextet 3	0.24	-0.12	25.2	18.9	ε-Fe_2O_3
Sextet 2	0.38	-0.10	37.59	23.0	
Sextet 1	0.37	-0.19	43.53	18.7	

Magnetic characterization

In order to correlate the incommensurate magnetic transition with the structural distortions of the different Fe^{3+} sites, it is necessary to determine the magnetic properties of these nanoparticles and establish the range temperature where they go across this magnetic transition observed at low temperatures. Figure 5a illustrates a magnetic hysteresis loop collected at RT under a maximum applied magnetic field of 50 kOe. The main magnetic features of the ε-phase are a huge maximum coercivity of 20 kOe observed at RT and the sample is not fully saturated even when applying an external magnetic field of 50 kOe [15].

In the present work, the saturation of the hysteresis loop is not fully reached with a maximum external magnetic field of 50 kOe, but the magnetic hysteresis loop shows a coercive field of 90 Oe. This value, well below the maximum reported coercivity of 20 kOe for epsilon iron oxide, might be because of the small nanoparticle size and the narrow size distribution obtained following this recipe at this synthesis temperature. The relationship between particle size and coercivity has been recently reported in powder samples by Ohkoshi et al. [44].

Their results show that for diameters below ~7.5 nm, ε-Fe_2O_3 behaves as a superparamagnetic material. From that size value, the material behaves as a ferromagnetic material and its coercivity increases with particle size, which reaches a value around 20 kOe when the size is over ~20 nm. In their work, the size distribution of the nanoparticles is relatively large, so they obtain more ε-particles which behave as a ferromagnetic material with large coercivities than in our work, where the particle size distribution is confined with diameters between ~7-15 nm, being the average particle size ~12 nm. The different mean size and tail distributions of the particles is the origin of the disparate coercivity values when comparing different works.

There are several differences in the synthesis method in our work with respect to other works. One of them is the annealing temperature of samples synthesized in this investigation, which is lower than that described also by Ohkoshi et al. [44]. Both recipes are quite different, and the influence of employing other concentrations and precursors into the solution might result in other thermal values to obtain the same properties for a specific particle size. Besides, in [44] the authors obtained powder samples and removed the SiO_2 matrix with a post-chemical etching process using a NaOH solution after the thermal treatment at high temperatures. In our case, we fabricate samples as a coating on a Si(100) substrate and surface tension effects or stress induced by the SiO_2 matrix on the nanoparticle seems to be the factors which might slightly modify the synthesis conditions previously reported [44].

To determine the magnetic populations which affect the shape and magnitude of the magnetic hysteresis loop, the derivative of the magnetization is calculated and represented in Figure 5b. The derivative shows an intense peak at ~0 kOe accompanied by two bumps with a maximum located at ~15 kOe. The intense peak is related to the ε-superparmagnetic population and the other bumps are associated to ε-Fe_2O_3 particles with larger sizes which have a ferromagnetic response.

The ZFC-FC curves show that the incommensurate magnetic order transition is located between 60 and 125 K (see Figure 5b). Due to the particle size, comprised between 7-15 nm, this transition is relatively broad and it is displaced towards lower temperatures if it is compared to other works with larger particle size [14]. According to the derivative of ZFC-FC curves, this transition has a maximum situated at ~100 K and no other magnetic transitions related to epsilon or other iron oxide polymorphs are detected. The magnetization difference found between ZFC and FC curves at RT indicates the presence of a ferromagnetic compound at RT (which is, on the other hand, seen in Figure 5a).

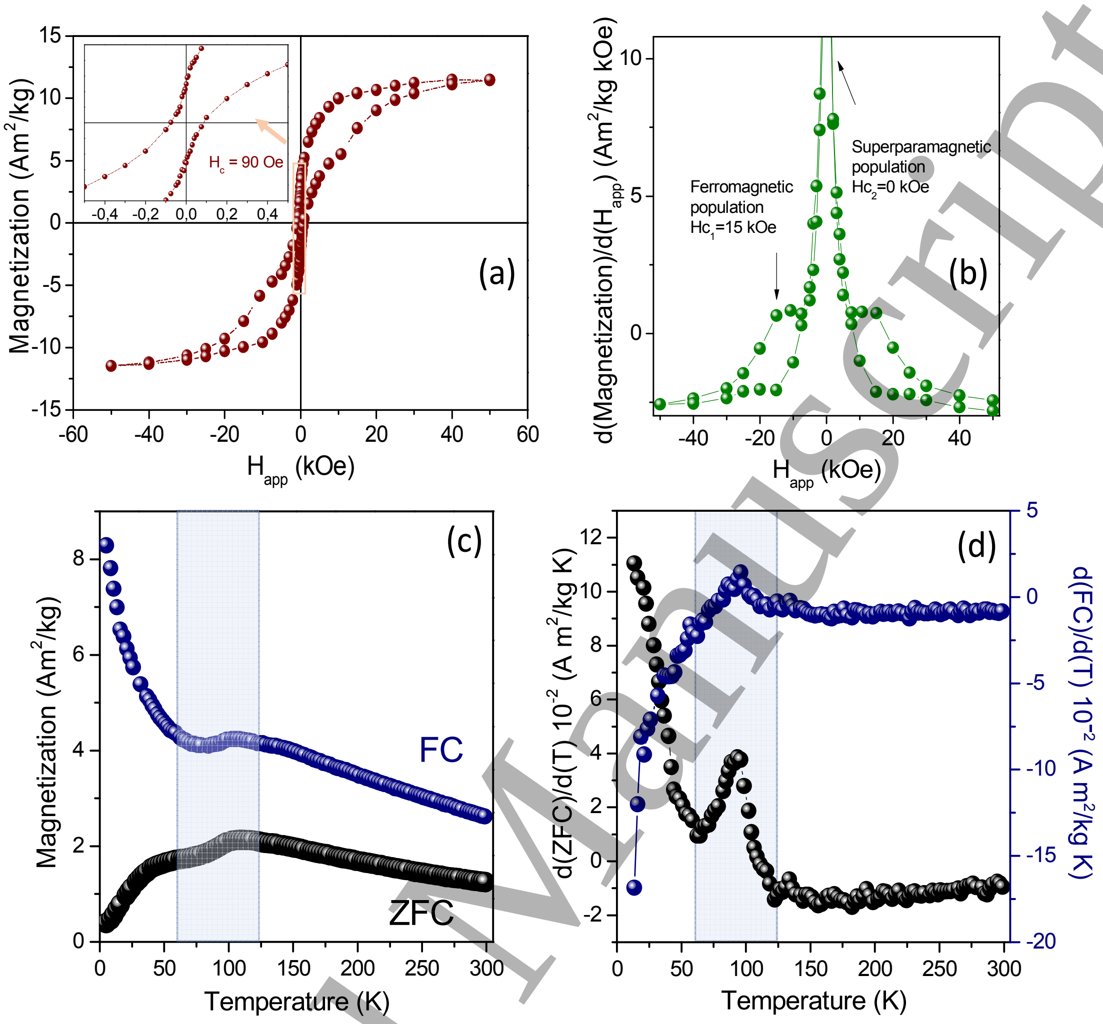

Figure 5. (a) Hysteresis magnetic loop collected at RT under a maximum applied magnetic field of 50 kOe. The inset displays a magnification of the central area; (b) d(Magnetization)/d(Happ) of the hysteresis loop acquired at 300 K; (c) ZFC-FC curves; (d) d(ZFC-FC)/d(T) curves showing the thermal evolution of magnetization for ε-nanoparticles.

Local structural distortion along the transition at 100 K of the ε-phase

ε-Fe_2O_3 goes through a second order structural transition originated from changes in coordination of Fe-D1$_{oc}$ and Fe$_{te}$ sites simultaneously with the emergence of an incommensurate magnetic order. These lattice distortions produce a strong reduction in the spin-orbit coupling registered by a dramatic decrease in the spin orbital momentum well reported in other works by combination of neutron and X-ray diffraction and X-ray magnetic circular dichroism experiments [30,45].

Concretely, the Fe-D1_{oc} and Fe_{te} polyhedral coordination back in the same (001) planes and share corners over a common oxygen atom where the Fe_{3d} and O_{2p} are overlapped. This effect promoted by the temperature induces displacements in the charge density of the Fe-D1_{oc} - Fe_{te} bonds increasing its ionic character [45]. The authors of the work suggest the changes in the charge density coming from the significant reduction in Fe-O bond length at about ~10% in agreement with Rietveld refinements and neutron diffraction patterns [45].

This phenomenon is also investigated by a Mössbauer experiment as a function of the temperature ranging from 10 to 200 K observing the same structural changes [30]. However, the atomic local order along this transition can be, in principle, more directly addressed by XAFS, allowing a more detailed temperature-dependent study. To understand the origin of the magnetic transition observed (see Figures 5c-d) between 60 K and 125 K for the ε-phase and its possible relationship with a local structural change, we perform a study of the behavior of the local structure of Fe by XAFS. The variations in the local structure parameters have been monitored *in situ* along the transition cooling down and heating up in a He-L cryostat. The high purity of the samples permits to assign the characteristics of the spectra solely to this phase.

The RT X-ray absorption near edge structure (XANES) spectrum at the K-Fe edge for the ε-Fe_2O_3 nanoparticles embedded in the silica matrix is presented in Figure 6a. XANES spectra for hematite and maghemite reference powders are shown as well. The main features of the spectrum are the presence of an intense pre-peak (common to Fe oxides [46]), and a well-defined main absorption peak with a sharp shape on the top and a second resonance around 7145 eV [15].

The XANES spectra illustrated in the Figure 6a show that the shape of the absorption peak and the secondary resonances are slightly different between them, since they have different crystal structure and the charge density is different in each compound. The α-Fe_2O_3 XANES spectrum has a double-peak shape in the absorption peak which differs from the others. Regarding the γ-Fe_2O_3 absorption peak, it is sharper than that of ε-Fe_2O_3 and much more than for α-Fe_2O_3. ε-Fe_2O_3 seems to be an intermediate compound between γ-Fe_2O_3 and α-Fe_2O_3 considering the XANES features. Generally speaking, one can distinguish different polymorphs observing the XANES characteristics [47].

The temperature dependent extended XAFS experiment is carried out in the range between RT and 10 K, keeping thermalization times at each condition between 10-30 min with four spectra acquired at each temperature. The EXAFS spectra in wave-vector space (k-space) of the sample in the range of temperatures studied are presented in Figure 6b. Despite the noise at k values higher than 10 Å, the oscillations are clearly observed upon k values of 10.5 $Å^{-1}$. However, as mentioned earlier, we restrict the fitting range up to 8.7 $Å^{-1}$, for which the signal to noise ratio is reasonable.

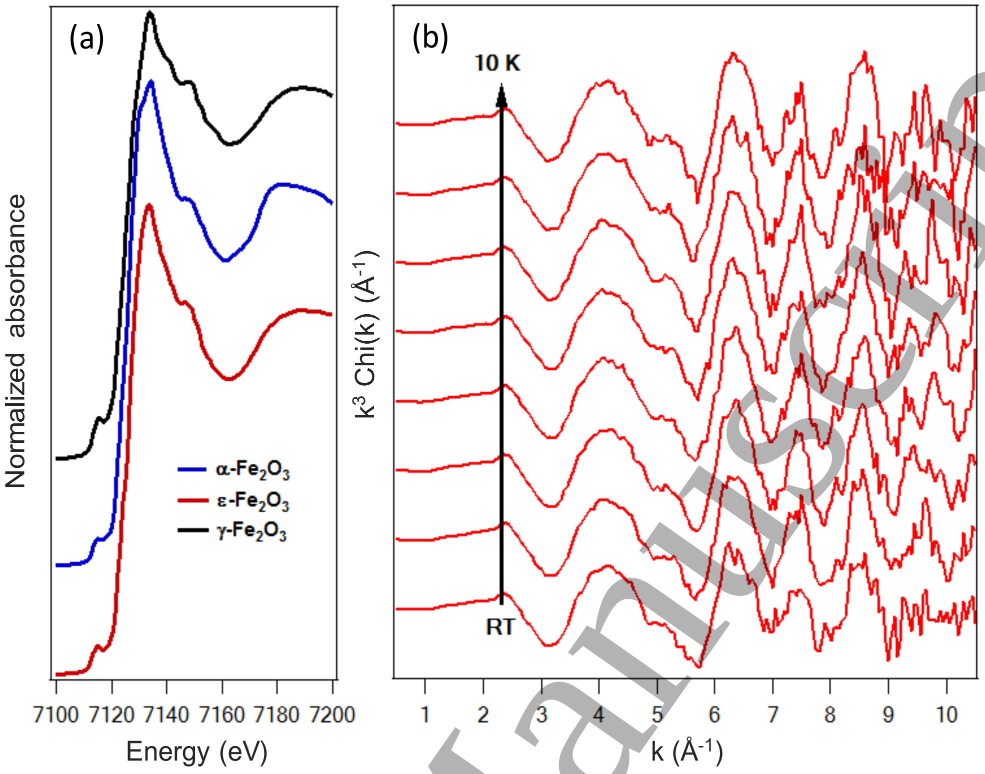

Figure 6. (a) XANES of γ-, α- and single phase ε-Fe_2O_3 acquired at RT conditions. γ- and α-Fe_2O_3 commercial powder references are added for comparison; (b) Temperature-dependent EXAFS spectra in the photoelectron wave-vector space of the ε-phase.

One of the structural fitting parameters is the relative variation of the shells distances respect of the crystallographic standard values. In Figure 7a we present the relative variation of shell distances, obtained as global parameter *a* in the model as a function of the temperature in the form:

$$R_{exp} = R_{cryst}\,(1 + a) \qquad [2]$$

Here the experimental bonding distance of each shell is calculated from the tabulated crystallographic bonding distance and adjusted with this global parameter which accounts for all the shell distance variations around the Fe center. The temperature dependence of this

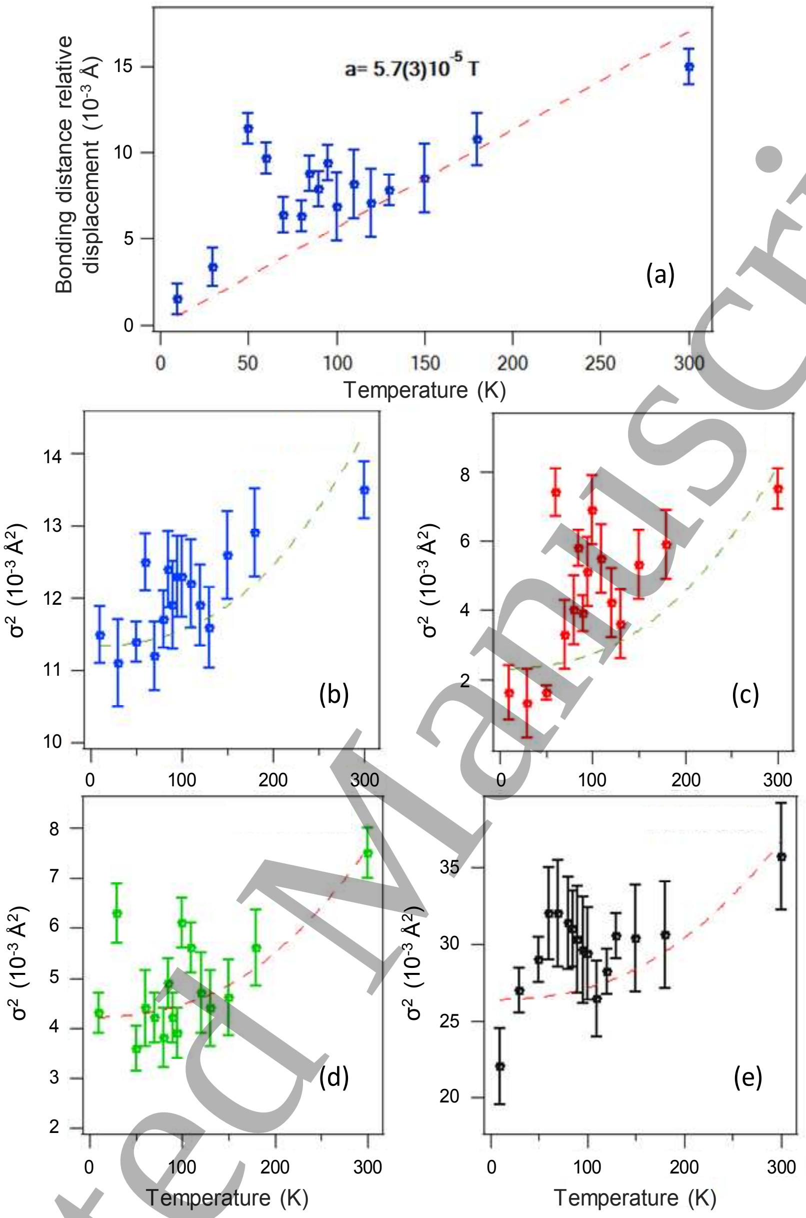

Figure 7. (a) Temperature dependence of the global bonding distance deviation parameter. The dashed line represents the fitting to a linear function. In the graph, the calculated thermal dependence coefficient is indicated; Temperature-dependent Debye-Waller factor calculated for the first four shells of the Fe in ε-Fe_2O_3: Fe-O1 (b), Fe-O2 (c), Fe-Fe1 (d) and Fe-Fe2(e).

parameter can be roughly thought as a thermal expansion coefficient around the Fe sites. As the Figure 7a shows, the monotonic increase of the experimental points does not fulfill a linear behavior. An abrupt deviation from the linearity is observed in the range from 60-125 K coinciding with the range temperatures in which the coercive field quenching is suggested. Consequently, we propose that this local bonding distance distortion is related to the magnetic phase transition.

As before mentioned, Fe in ε-Fe_2O_3 is placed in four different sites: Fe-R_{oc}, Fe-D1,2_{oc}, $Fe4_{te}$ (Figure 4a). Considering current limitations in the spatial resolution of the shells and the existence of the different cation sites, we are not able to clearly distinguish between O shells for the different octahedral Fe sites if their differences lie within the above-cited lower limit of 0.18 Å. Nevertheless, regarding the coexistence of the different cation sites and the incidence of each one in the lattice, we can infer (on average) that the first O shell (with four atoms) should be addressed to the octahedral oxygen and the second one to the tetrahedral one in our model. This approximation fits well with the relative amount of each O in the unit cell, where the O in tetrahedral corners represents about 1/5 of the total number of O atoms.

The global parameter for the relative bonding distance distortion does not account for the origin of the structural shifts for individual sites. In this sense, the DW parameter of each sub-shell reports the deviations of each particular sub-shell from the expected value of the bond distance. The DW is strictly the variance of the expected bonding distance of a particular shell. Such parameter includes two different terms: static (σ_S) and dynamic (σ_D) contributions. The first one does not depend on temperature. However, the second one has a temperature dependence which follows the correlated Debye-like behavior [48].

$$\sigma_D^2 = \frac{3h^2}{M k_B \theta_D}\left(\frac{1}{4} + \left(\frac{T}{\theta_D}\right)^2 \int_0^{\theta_D/T} dx \frac{x}{e^x - 1}\right) \qquad [3]$$

Thus, one can calculate and predict the Debye temperature by fitting the temperature dependence of the DW factor to this relation. θ_D is the Debye temperature and M is the mass of the scattering atom. Therefore, deviations from the DW curve can be understood as originated by additional sources of atomic disorder on a particular atomic shell. The temperature dependencies of the DW factors for the two Fe-O sub-shells are represented in Figure 7b-c.

The σ^2(T) curves for the O shells in Figures 7b-c show clear shoulders in both cases. The shoulder is more pronounced in the case of the single O second shell. In both cases, it seems to be well centered at 100 K, and is clearly distinguished from the monotonic Debye-like behavior. The larger intensity in the second O shell should be related to the assumption that this shell corresponds to the neighboring O in the tetrahedral Fe ions. Since the cations in these sites develop a larger distortion, as previously observed by Mössbauer and XRD techniques [14,30], this can be on the origin of such enhanced distortion. However, a clear deviation (lower in magnitude intensity) from the Debye model is also observed for the first O shell, which accounts as a merge of contributions of octahedral and tetrahedral sites. It should be stressed that in this case the difference in the intensity of the distortion points out at a higher order effect in the O placed on tetrahedral coordination. A similar behavior is observed for the Fe shells and is reported in the Figures 7d-e. Roughly, the discontinuity seems to be similar in both cases, but is somehow weaker in the Fe-Fe shells. In part, it could be explained by the very local nature of EXAFS signal, which has more sensitivity for the inner shells distortion than for the outer shells.

The calculated DW of the different shells as a function of temperature is fitted using Equation 3 [49]. The curves at the Figures 7b-d show the fitting of the data in case of the Fe-O1 (b), Fe-O2 (c), Fe-Fe1 and Fe-Fe2 of the temperature dependency of DW parameter. The parameters calculated in the fittings are summarized in Table 2.

Table 2. Debye temperatures and static offset (σ_S) term calculated from the fitting of the temperature dependent DW curves for the four first shells.

Shell	Debye Temperature-θ_D (K)	σ_S (Å^2)	R-coeff
Fe-O1	540 (30)	0.0104(2)	0.89
Fe-O2	490 (20)	0.0002(1)	0.87
Fe-Fe1	460 (20)	0.0030(5)	0.87
Fe-Fe2	400 (100)	0.0230(2)	0.82

The static contribution is the offset of the function and represents a static disorder inherent of the shell considered. The values calculated for the different shells (σ_S) present rather large values. As expected, the first Fe-O1 shell, which is formed by the contribution of many subshells (mainly from Fe in octahedral sites) presents a high variance of the mean value. In the opposite case, the Fe-O2 shell which is formed by a single O atom presents a much lower static disorder. Regarding the Fe-Fe shells, quite high values are obtained as well (Table 2). In case of the Fe-Fe shells the situation is the opposite and the nearest one presents a lower static disorder. The larger disorder in the shell located farther may be also related to the finite size of the nanoparticle size, which should limit the medium and long range order observed. Following the Debye model for atomic oscillators in a solid, the Debye temperature correlative to each atomic shell is a measurement of the bond strength. For instance, the θ_D of the Fe-O1 shell gives the order of the stability of this shell. In the current case, it can be observed that, within the experimental error, the Debye temperatures of the Fe-O shells are slightly higher than those of the Fe-Fe. However, the range of values lies well within the tabulated values for iron oxides [50].

In the case of the second Fe shell (Figure 7e), the temperature-dependent DW factor, shows a broad shoulder center located around 60-70 K (thus lower than 100 K). This shoulder center position almost coincides with the temperature observed for the bump in the thermal expansion coefficient (TEC) and the starting point of the transition observed in the derivative ZFC-FC curves (Figure 5). The interesting effect corresponding to this second Fe shell is that the DW factor trend with temperature begins to increase before the magnetic transition temperature appeared. The path length for this second Fe shell is associated to the interaction of the Fe_{te} with Fe-$D1_{oc}$ polyhedrons. This interaction takes place towards lower temperatures and seems to be the precursor stage to promote the magnetic transition compared to the first Fe shell which is associated to the interaction between Fe_{te}-Fe_{te} and Fe-R_{oc}, Fe-D1-2_{oc} each other. In the representation of DW factor corresponding to the first Fe shell are detected the same anomalies (in temperature) as those observed in the Fe-O shells around 100 K (Figures 7b-d). On the other hand, the anomalies in the DW factor in the second Fe shell are much obvious towards lower temperatures and this second Fe shell might be sensitive to the particle size in this nanometric range (7-15 nm). The particles with less size go through the magnetic transition before than the largest ones. This interpretation might explain the broad trend of the DW factor accompanied with the anomalies detected are displaced toward lower temperatures than 100 K. Interestingly, these structural distortions are observable dealing with ε-nanoparticles with a global coercivity of ~90 Oe. One could expect less structural deviations since the magnetic transition is softer and broaden than one coming from nanoparticles with larger sizes [14]. To conclude, we propose that the interaction of the Fe_{te} with Fe-$D1_{oc}$ polyhedrons are the seed mechanism of the magnetic transition promoted by temperature. This proposal is suggested working with these nanoparticle sizes wherein the structural distortions are likely moderate due to surface effects.

Conclusions

ε-Fe_2O_3 nanoparticles enclosed in a silica matrix thin film on a Si(100) substrate are synthesized following a novel one-pot sol-gel recipe, which provides a particle size distribution between 7 and 15 nm. From the analysis of the Mössbauer spectrum collected at RT, the percentage of the ε-polymorph in the sample is, nominally, 100%. The magnetic transition around 100 K is investigated, and the origin of this magnetic anomaly is analysed by XAFS. We report a different structural behavior depending on the examined sub-shell. We distinguish one bump with a trend which deviates from the Debye-like behavior, representing the DW factor as a function of the temperature for the first sub-shells of Fe-O1,2 and Fe-Fe1,2. The maximum structural distortion is almost coincident in temperature (~100 K) for Fe-O1,2 and Fe-Fe1 sub-shells. Thus, the bumps observed fall in the same temperature range as the magnetic transition occurs. Consequently, these structural modifications are linked along the magnetic transition. Surprisingly, the structural changes in the Fe-Fe2 sub-shell start at lower temperatures than the emergence of the collinear ferrimagnetic state and the maximum of the bump is displaced to ~65 K. This means the magnetic and structural changes are uncoupled in the Fe-Fe2 sub-shell in a certain range of temperature for ε-nanoparticles with sizes of few nanometers (7-15 nm) where, probably, the surface effects are dominant. We suggest that these local interactions between the Fe_{te} with Fe-$D1_{oc}$ polyhedrons may be the seed mechanism of the long-range structural transformation, which, in turn, is associated to the magnetic order transition from the incommensurate magnetic order to the collinear ferrimagnetic order.

Acknowledgements

This work is supported by the Ministerio Español de Economía y Competitividad (MINECO) through the projects MAT2012-38045-C04-03, MAT2015-64110-C2-1-P, MAT2013-48009-C04-01-P, MAT2015-66888-C3-3-R and FIS-2008-06249. Financial support from Fundación BBVA is also acknowledged. J. L.-S. thank the FPI fellowship. The ESRF, MINECO and CSIC are acknowledged for provision of synchrotron radiation facilities and the financial support for the beamtime (PIE-2010-OE-O13-200014). We would like to thank the BM25-SpLine staff for the technical support beyond their duties.

References

[1] Zboril R, Mashlan M and Petridis D 2002 *Chem. Mater.* **14** 969–82

[2] MacHala L, Tuček J and Zbořil R 2011 *Chem. Mater.* **23** 3255–72.

[3] Jones N 2011 *Nature* **472** 22–3.

[4] Yoshikiyo M, Namai A and Ohkoshi S 2013 *Ferromagnetic Resonance - Theory and Applications* ed O Yaln (InTech).

[5] Namai A and Ohkoshi S 2011 *Advanced Trends in Wireless Communications* vol 3, ed M Khatib (InTech).

[6] Korte D, Carraro G, Maccato C and Franko M 2015 *Opt. Mater.* **42** 370–5.

[7] Gich M, Frontera C, Roig A, Molins E, Fontcuberta J, Bellido N, Simon C and Fleta C 2006 *Nanotechnology* **17** 687–91.

[8] Gich M, Fina I, Morelli A, Sánchez F, Alexe M, Gàzquez J, Fontcuberta J and Roig A 2014 *Adv. Mater.* **3** 4645–52.

[9] Gich M, Gazquez J, Roig A, Crespi A, Fontcuberta J, Idrobo J C, Pennycook S J, Varela M, Skumryev V and Varela M 2010 *Appl. Phys. Lett.* **96** 2008–11.

[10] Carraro G, Barreca D, Maccato C, Bontempi E, Depero L E, de Julián Fernández C and Caneschi A 2013 *CrystEngComm* **15** 1039.

[11] Battisha I K, Afify H H and Hamada I M 2005 *J. Magn. Magn. Mater.* **292** 440–6.

[12] Tadić M, Spasojević V, Kusigerski V, Marković D and Remškar M 2008 *Scr. Mater.* **58** 703–6.

[13] Kurmoo M, Rehspringer J-L, Hutlova A, D'Orléans C, Vilminot S A, Estournes C and Niznansky D 2005 *Chem. Mater.* **17** 1106–14.

[14] Gich M, Roig A, Frontera C, Molins E, Sort J, Popovici M, Chouteau G, Martín y Marero D and Nogués J 2005 *J. Appl. Phys.* **98** 1–5.

[15] López-Sánchez J, Muñoz-Noval A, Serrano A, Abuín M, de la Figuera J, Marco J F, Perez L, Carmona N and Rodríguez de la Fuente O 2016 *RSC Adv.* **6** 46380.

[16] López-Sánchez J, Serrano A, Del Campo A, Abuín M, Rodríguez de la Fuente O and Carmona N 2016 *Chem. Mater.* **28** 511–8.

[17] Nikolic V N, Spasojevic V, Panjan M, Kopanja L, Mrakovic A and Tadic M 2017 *Ceram. Int.* **43** 7497–507.

[18] Nikolić V N, Tadić M, Panjan M, Kopanja L, Cvjetićanin N and Spasojević V 2017 *Ceram. Int.* **43** 3147–55.

[19] Tadic M, Milosevic I, Kralj S, Mitric M, Makovec D, Saboungi M-L and Motte L 2017 *Nanoscale* **9** 10579–84.

[20] Yoshikiyo M, Namai A, Nakagawa K and Ohkoshi S 2017 *AIP Adv.* **7** 56218.

[21] Ohkoshi S I, Sakurai S, Jin J and Hashimoto K 2005 *J. Appl. Phys.* **97** 8–11.

[22] Tucek J, Ohkoshi S I and Zboril R 2011 *Appl. Phys. Lett.* **99** 2012–5.

[23] Sakurai S, Tomita K, Hashimoto K, Yashiro H and Ohkoshi S 2008 *J. Phys. Chem. C* **112** 20212–6.

[24] Sakurai S, Shimoyama J I, Hashimoto K and Ohkoshi S I 2008 *Chem. Phys. Lett.* **458** 333–6.

[25] Jin J, Ohkoshi S and Hashimoto K 2004 *Adv. Mater.* **16** 48–51.

[26] Mohapatra M and Anand S 2010 *Int. J. Eng. Sci. Tech.* **2** 127–46.

[27] Rao A V and Kulkarni M M 2002 *Mater. Chem. Phys.* **77** 819–25.

[28] Kim C E, Yoon J S and Hwang H J 2009 *JSST* **49** 47–52.

[29] Tuček J, Zbořil R, Namai A and Ohkoshi S I 2010 *Chem. Mater.* **22** 6483–505.

[30] Gich M, Frontera C, Roig A, Taboada E, Molins E, Rechenberg H R, Ardisson J D, Macedo W A A, Ritter C, Hardy V, Sort J, Skumryev V and Nogués J 2006 *Chem. Mater.* **3** 3889–97.

[31] Kohout J, Brázda P, Závěta K, Kubániová D, Kmječ T, Kubíčková L, Klementová M, Šantavá E and Lančok A 2015 *J. Appl. Phys.* **117** 2–6.

[32] Horcas I, Fernández R, Gómez-Rodríguez, J. M., Colchero J, Gómez-Herrero J and Baro A M 2007 *Rev. Sci. Instrum.* **78** 13705.

[33] Rubio-Zuazo J, Collado-Negro V, Heyman C, Ferrer P, Silva I da, Gallastegui J A, Gutiérrez-León A and Castro G R 2013 *J. Phys. Conf. Ser.* **425** 52005.

[34] Ravel B and Newville M 2005 *J. Synchrotron Radiat.* **12** 537–41.

[35] Ankudinov a. L, Rehr J J and Conradson S D 1998 *Phys. Rev. B* **58** 7565–76.

[36] Lavrentyev A A, Nikiforov I Y, Dubeiko V A, Gabrelian B V. and Rehr J J 2001 *J. Synchrotron Radiat.* **8** 288–90.

[37] Kelm K and Mader W 2005 *ZAAC* **631** 2383–9.

[38] Brázda P, Kohout J, Bezdička P and Kmječ T 2014 *Cryst. Growth Des.* **14** 1039–46.

[39] Namai A, Yoshikiyo M, Yamada K, Sakurai S, Goto T, Yoshida T, Miyazaki T, Nakajima M, Suemoto T, Tokoro H and Ohkoshi S 2012 *Nat. Comm.* **3** 1035.

[40] Popovici M, Niz D, Roig A, Savii C, Molins E, Zaveta K, Enache C, Sort J, Brion S De, Chouteau G and Nogue J 2004 *Chem. Mater.* **16** 5542–8.

[41] Brázda P, Nižňanský D, Rehspringer J-L and Vejpravová J P 2009 *JSST* **51** 78–83.

[42] Pankhurst Q A, Johnson C E and Thomas M F 1986 *J. Phys. C* **19** 7081–98.

[43] Morales M P, Serna C J, Bødker F and Mørup S 1997 *J. Phys.: Condens. Matter* **9** 5461–7.

[44] Ohkoshi S-I, Namai A, Imoto K, Yoshikiyo M, Tarora W, Nakagawa K, Komine M, Miyamoto Y, Nasu T, Oka S and Tokoro H 2015 *Sci. Rep.* **5** 14414.

[45] Tseng Y-C, Souza-Neto N M, Haskel D, Gich M, Frontera C, Roig A, van Veenendaal M and Nogués J 2009 *Phys. Rev. B* **79** 94404.

[46] Corrias A, Ennas G, Mountjoy G and Paschina G 2010 *PCCP* 1045–50.

[47] Espinosa A, Serrano A, Llavona A, Jimenez de la Morena J, Abuin M, Figuerola A, Pellegrino T, Fernández J F, Garcia-Hernandez M, Castro G R and Garcia M A 2011 *Meas. Sci. Technol.* **23** 15602

[48] Beni G and Platzman P M 1976 *Phys. Rev. B* **14** 1514–8.

[49] Paolone A, Castellano C, Cantelli R, Rousse G and Masquelier C 2003 *Phys. Rev. B* **68** 14108.

[50] Dwight E. Gray and Bruce H. Billings 1972 American Institute of Physics handbook, *McGraw-Hill.*